How to cite: *Angew. Chem. Int. Ed.* **2024**, *63*, e202319091
doi.org/10.1002/anie.202319091

Zn-Ion Batteries

Interfacial Engineering of Zn Metal via a Localized Conjugated Layer for Highly Reversible Aqueous Zinc Ion Battery

Zhenjie Liu[+], Guanjie Li[+], Murong Xi[+], Yudai Huang, Haobo Li, Huanyu Jin, Juan Ding, Shilin Zhang,* Chaofeng Zhang,* and Zaiping Guo**

Abstract: Aqueous zinc-ion batteries are regarded as promising and efficient energy storage systems owing to remarkable safety and satisfactory capacity. Nevertheless, the instability of zinc metal anodes, characterized by issues such as dendrite growth and parasitic side reactions, poses a significant barrier to widespread applications. Herein, we address this challenge by designing a localized conjugated structure comprising a cyclic polyacrylonitrile polymer (CPANZ), induced by a Zn^{2+}-based Lewis acid (zinc trifluoromethylsulfonate) at a temperature of 120 °C. The CPANZ layer on the Zn anode, enriched with appropriate pyridine nitrogen-rich groups (conjugated cyclic –C=N–), exhibits a notable affinity for Zn^{2+} with ample deposition sites. This zincophilic skeleton not only serves as a protective layer to guide the deposition of Zn^{2+} but also functions as proton channel blocker, regulating the proton flux to mitigate the hydrogen evolution. Additionally, the strong adhesion strength of the CPANZ layer guarantees its sustained protection to the Zn metal during long-term cycling. As a result, the modified zinc electrode demonstrates long cycle life and high durability in both half-cell and pouch cells. These findings present a feasible approach to designing high performance aqueous anodes by introducing a localized conjugated layer.

Introduction

Renewable energy resources, including solar, wind, and tidal energy, have attracted significant attention over the past two decades. One of the critical challenges is how to direct use renewable energy resources due to their discontinuous, uncontrollable, and unstable generation.[1] Therefore, there is an urgent need for advanced energy storage system to serve as a medium for regulating electricity output and enhancing the ability of power grid to tolerate fluctuations in renewable energy.[2] Among next-generation energy storage systems, aqueous zinc ion batteries (AZIBs) hold great promise in large-scale energy storage due to high theoretical capacity of Zn metal (820 $mAh\,g^{-1}$ and 5855 $mAh\,cm^{-3}$) and aqueous electrolyte with safety and cost-effectiveness features.[3]

There has been rapid development in cathode design for AZIBs. However, further advancement is hindered by the poor cycling performance of the Zn anode, which is attributed to problematic issues such as dendrite growth and parasitic side reactions, including chemical corrosion and hydrogen evolution reaction (HER).[4] Several strategies have been explored and developed to tackle these problems, including 1) developing new substrate to regulate localized electric field to influence the Zn diffusion behaviour;[5] 2) introducing a functional interfacial layer to regulate Zn deposition;[6] 3) electrolyte engineering to guide the following zinc growth.[7] Among them, interface engineering is one of promising approaches to spatially guide the uniform Zn^{2+} ion flux and mitigate the dendrite growth. Zhao et al.[6b] designed a heteroanionic zinc ion conductor ($Zn_yO_{1-x}F_x$) interphase with fast Zn^{2+} transference kinetics. Wang et al.[6c] prepared a Zn-coordinated interphase (H-ZnCND) to regulate Zn deposition and stabilize Zn anodes. Unfortunately, though recently developed interface modification materials have greatly improved the life of Zn anodes, they still show an unsatisfactory effect in the suppression of side reactions.[8] The reported approaches often fail to achieve uniform ion distribution, high Zn^{2+} but low H^+ transfer number, and stable pH environment. This limitation results in challenges to achieve substantial improvements in cycling

[*] Z. Liu,[+] M. Xi,[+] Y. Huang, J. Ding
State Key Laboratory of Chemistry and Utilization of Carbon Based Energy Resources, College of Chemistry, Xinjiang University
Urumqi 830017, Xinjiang, China
E-mail: huangyd@xju.edu.cn

G. Li,[+] H. Li, H. Jin, S. Zhang, Z. Guo
School of Chemical Engineering, The University of Adelaide
Engineering North, North Terrace Campus, the University of Adelaide, Adelaide, South Australia, 5069, Australia
E-mail: shilin.zhang01@adelaide.edu.au
zaiping.guo@adelaide.edu.au

C. Zhang
Institutes of Physical Science and Information Technology, Leibniz Joint Research Center of Materials Sciences, Engineering Laboratory of High-Performance Waterborne Polymer Materials of Anhui Province, Anhui Graphene Engineering Laboratory, Key Laboratory of Structure and Functional Regulation of Hybrid Material (Ministry of Education), Anhui University, Hefei, 230601 China
E-mail: cfz@ahu.edu.cn

[+] These authors contributed equally to this work.

performance under low current density and low-capacity cycling conditions.

In this study, we employ a novel approach involving a Lewis acidic zinc salt (zinc trifluoromethylsulfonate, Zn-$(OTf)_2$)-assisted low-temperature cyclization strategy, which facilitates a pre-zincification process of polyacrylonitrile (PAN)-based Zn^{2+} transport layer materials (CPANZ). The cyclization process enables the systematically transforming of –C≡N bond in PAN to a ladder-like polymer structure with pyridine nitrogen-rich (conjugated cyclic –C=N) in CPANZ. For the first time, we use this pre-zincification process to regulate the behaviour of Zn with mitigated side reactions. The CPANZ layer tightly bonds with the Zn substrate by means of the high affinity of pyridine nitrogen with Zn atoms. Importantly, this coating layer acts as a Zn^{2+} transport layer and effective proton shield to prevent Zn corrosion and HER in aqueous electrolytes. As a result, the CPANZ interface-protected Zn anode demonstrates exceptional long cycling stability of over 6,000 hours at 0.5 mA cm^{-2} with a capacity of 0.5 mAh cm^{-2} and remarkable cycling performance at current densities of 1.0 and 3.0 mA cm^{-2}, respectively. The as-assembled full cells and hybrid capacitors exhibit high-capacity retention and superior Coulombic efficiency (CE) close to 100 % after 4,000 and 10,000 cycles at a current density of 4 mA cm^{-2} and 5 A g^{-1}, respectively. Our findings offer general principles for designing functional interfacial layers for AZIBs with long service life.

Results and Discussion

The change in colour is an indicator for the initiation of the cyclization reaction, in which the deeper the colour, the higher the degree of cyclization.[9] Figure 1a shows the colour change during the cyclization reaction of PAN with

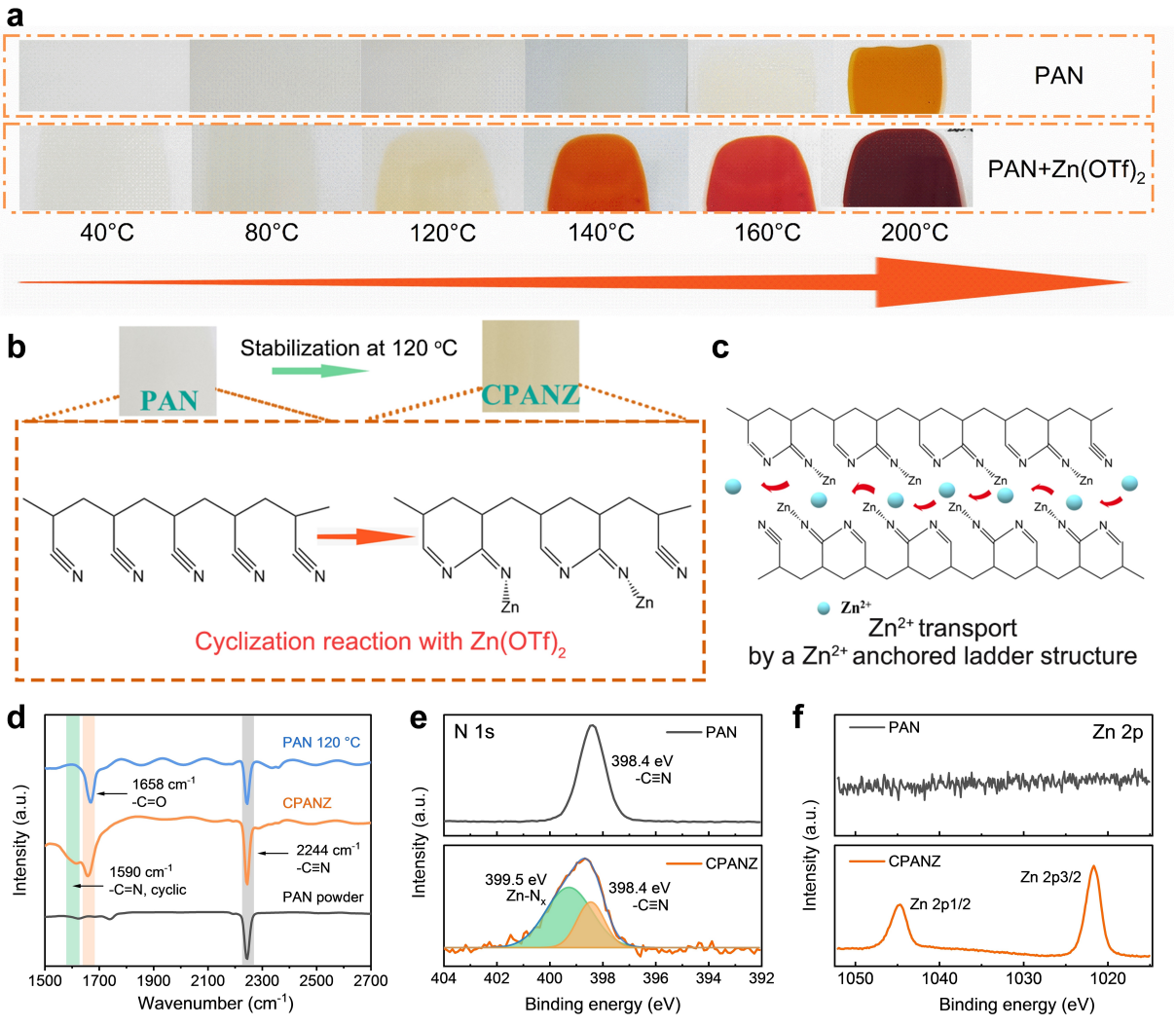

Figure 1. (a) Optical photos of PAN-based films obtained at different temperatures. (b) Schematic diagram of the $Zn(OTf)_2$-induced cyclization reaction of PAN, CPANZ is denoted as the PAN + $Zn(OTf)_2$ film after 120 °C treatment. (c) Schematic diagram of the transport mechanism of Zn^{2+} in the cyclized PAN with a conjugated structure. (d) FT-IR spectra of PAN and localized conjugated CPANZ film. (e) N 1s and (f) Zn 2p XPS spectra of PAN and CPANZ film.

or without $Zn(OTf)_2$. Notably, when $Zn(OTf)_2$ is added, the colour change starts at a lower temperature of 120 °C, compared to pure PAN without the $Zn(OTf)_2$ additive (200 °C). This indicates that the introduction of $Zn(OTf)_2$ salt accelerates the cyclization process of PAN. The strong Lewis acidity of $Zn(OTf)_2$ can act as a catalyst to facilitate the intramolecular cyclization,[10] which is consistent with previous reports on the using of catalyst to reduce the cyclization temperature of PAN.[9b,11] We further use density functional theory (DFT) calculation to further understand the underlying mechanism. Figure S1 illustrates the coordination between OTf^- anions and PAN monomers, which results in the redistribution of electron density in the PAN molecule. This redistribution contributes to an increase in the energy level of the highest occupied molecular orbit (HOMO), making it more prone to lose valence electrons. During the cyclization process, the –C≡N bond transforms to a –C=N– bond, creating a partial conjugated structure (Figure 1b), which enhances molecular stability and Zn^{2+} conduction (Figure 1c).[12] Specifically, the anchored Zn^{2+} selectively coordinates/fixes with the N atom in the –C=N– trapezoidal structure and binding with surrounding anions, resulting in guest Zn^{2+} to jump between active sites anchored to the main skeleton. To verify the effect of $Zn(OTf)_2$ and the chemical change of the PAN film with $Zn(OTf)_2$ after high-temperature treatment, thermogravimetric-differential thermal analysis (TG-DTA) and Fourier transform infrared (FT-IR) spectroscopy were conducted. As shown in Figure S2a, the PAN film exhibits an exothermic peak beginning at about 200 °C, representing oxidation and cyclization reactions.[11] In contrast, the exothermic peak in the PAN + $Zn(OTf)_2$ film begins to show at a lower temperature of about 150 °C (Figure S2b), further confirming that $Zn(OTf)_2$ can reduce the energy barrier of oxidation and cyclization reactions of PAN. Similar results can be also obtained for TG-DTA conducted in N_2 atmosphere (Figure S3). The exothermic peak in the PAN + $Zn(OTf)_2$ film is observed to be less distinct, suggesting a more moderated cyclization reaction in comparison to the PAN film. The PAN + $Zn(OTf)_2$ film after heat treatment at 80 °C and 120 °C are denoted as PANZ and CPANZ film, respectively.

Analysis of FT-IR spectra (Figure 1d) indicates a peak associated with –C=N emerges at 1,590 cm^{-1} in CPANZ, providing evidence of the successful cyclization of PAN.[12] Additionally, the distinct peak at 2,244 cm^{-1}, corresponding to the –C≡N stretching is remained in the CPANZ, indicating the partial cyclization of the PAN skeleton. The peak observed at 1,658 cm^{-1} in both CPANZ and PAN samples can be attributed to the formation of the –C=O band, indicating the oxidation of the skeleton. The local chemical environment of CPANZ is further characterized by the X-ray photoelectron spectroscopy (XPS) spectra (Figure 1e, f, Figure S4–S5). The emerged peak at 399.5 eV in Figure 1e can be attributed to the Zn-N_x species, indicating the successful binding between Zn^{2+} and –C=N in CPANZ.[13]

The ionic conductivities of localized conjugated CPANZ film are illustrated in Figure S6. Elevating the temperature to 120 °C contributes to an increase in ionic conductivity due to the formation of a localized conjugated structure (conjugated cyclic –C=N). The CPANZ obtained at 120 °C (denoted as CPANZ-120) exhibits the highest ionic conductivity of 1.183 mS cm^{-1} (Figure S6). Notably, the ionic conductivity decreases when the treatment temperature exceeds 140 °C due to over-cyclization of the PAN chain segments. Despite achieving higher rigidity, the migration of Zn^{2+} in the polymer segments becomes significantly slower. Considering that the primary function of the CPANZ interfacial layer is to harness Zn^{2+} flux and proton migration, high ionic conductivity is crucial. Because of the highest ionic conductivity, the CPANZ obtained at 120 °C is regarded as an efficient Zn^{2+} conductor, making it suitable for further investigations in AZIBs. Using a facile doctor-blading method, we prepared CPANZ@Zn anodes and used them for AZIBs. The localized conjugated CPANZ layer on the Zn anode exhibits a dense surface and a uniform thickness of 6 μm (Figure S7–S8). The compact surface ensures efficient electronic isolation, facilitating the passivation of the Zn anode and suppression of side reactions. The kinetics of bare Zn, PANZ@Zn, and CPANZ@Zn anodes were determined using temperature-dependent electrochemical impedance spectroscopy (EIS, Figure S9 and S10). According to fitted results, the activation energy of charge transfer resistance (R_{ct}) in the CPANZ@Zn anode is 0.198 eV, which is lower than that of PANZ@Zn (0.275 eV) and bare Zn (0.303 eV). The low activation energy indicates that the Zn^{2+} migration follows the Grotthuss hopping mechanism, in which the guest Zn^{2+} jumps from a stationary –C=N– site to a neighbouring –C=N– site in the cyclized PAN skeleton.[12] Due to the fast migration kinetics, the Zn^{2+} transference number ($t_{Zn^{2+}}$) of the CPANZ layer is increased to 0.778, which is higher than those of PANZ@Zn (0.582) and bare Zn (0.256) (Figure S11). This improved Zn^{2+} migration behaviour can help to achieve a rapid desolvation process and a more uniform Zn^{2+} flux, which will contribute to a uniform Zn electrodeposition.[14] Importantly, in comparison to the H^+, the Zn^{2+} exhibits a preference for bonding with –C=N– sites of the localized conjugated CPANZ due to its higher charge density. The Zn^{2+} anchored in the CPANZ layer introduces strong electrostatic repulsion against the H^+, reducing proton density and disrupting the proton migration path within the CPANZ layer.[12] This can be further evidenced by the higher impedance observed in the HOTf//CPANZ//HOTf cell in contrast to the $Zn(OTf)_2$//CPANZ//$Zn(OTf)_2$ cell (Figure S12). It confirms that proton migration is slower than Zn^{2+} migration within the CPANZ layer. Furthermore, we investigated proton migration in the CPANZ film using an H-cell. As shown in Figure S13, two chambers that were individually filled with 1 M H_2SO_4 or pure deionized water, separated by PANZ and CPANZ films. In the PANZ cell, the pH value of the deionized water chamber decreases to 1.06 after 12 hours due to the diffusion of proton from the 1 M H_2SO_4 chamber. In contrast, the pH value maintains a moderate value of 4.04 in the water chamber of the CPANZ cell, demonstrating the excellent suppression of proton migration by CPANZ film. This result implies that the

CPANZ@Zn electrode can mitigate the HER side reactions and owns good anti-corrosion capacity. The mitigated HER were further examined by using the linear sweep voltammetry in NaOTf electrolyte, which aims to eliminate the interference of Zn deposition at the specific potential. The HER potential is defined as the potential at a current density of 1 mA cm^{-2}. As shown in Figure 2a, the HER potential is extended from −1.58 V (Bare Ti) to −1.67 V (CPANZ@Ti) in 1 M NaOTf electrolyte. Additionally, the corrosion of the Zn anode is suppressed, as evidenced by the lower corrosive current and higher corrosive potential observed in the Tafel curves (Figure 2b). Bare Zn and CPANZ@Zn electrodes were soaked in the 2 M $Zn(OTf)_2$ electrolyte for 14 days to monitor the evolution of the Zn surface. With the soaking time extended, the surface of the bare Zn gradually changed from a bright metallic colour to a dark grey colour, indicative of intensified corrosion reactions (Figure S14). Additionally, a large number of by-products were observed in the XRD pattern of the bare Zn electrodes after long-term storage (Figure S15). In contrast, CPANZ@Zn anodes maintained pristine pattern, with minimal by-product observed even after 14 days of storage. These findings substantiate the effective inhibition of Zn anode corrosion through the interfacial engineering introduced by the CPANZ layer. The CPANZ@Zn//CPANZ@Cu cell therefore exhibits an improved average Coulombic efficiency (ACE) of 99.4 % after 4000 cycles at a current density 1 mA cm^{-2} with a capacity of 0.1 mAh cm^{-2} (Figure 2c,d). The ACE remains above 99.1 % at a capacity of 1 mAh cm^{-2}, which is superior to those in bare Zn and PANZ@Zn anodes (Figure 2e,f and Figure S16). The improved reversibility of Zn plating/strippingin CPANZ@Zn anode can be attributed to the introduction of CPANZ layer, which mitigates side reactions and offers anti-

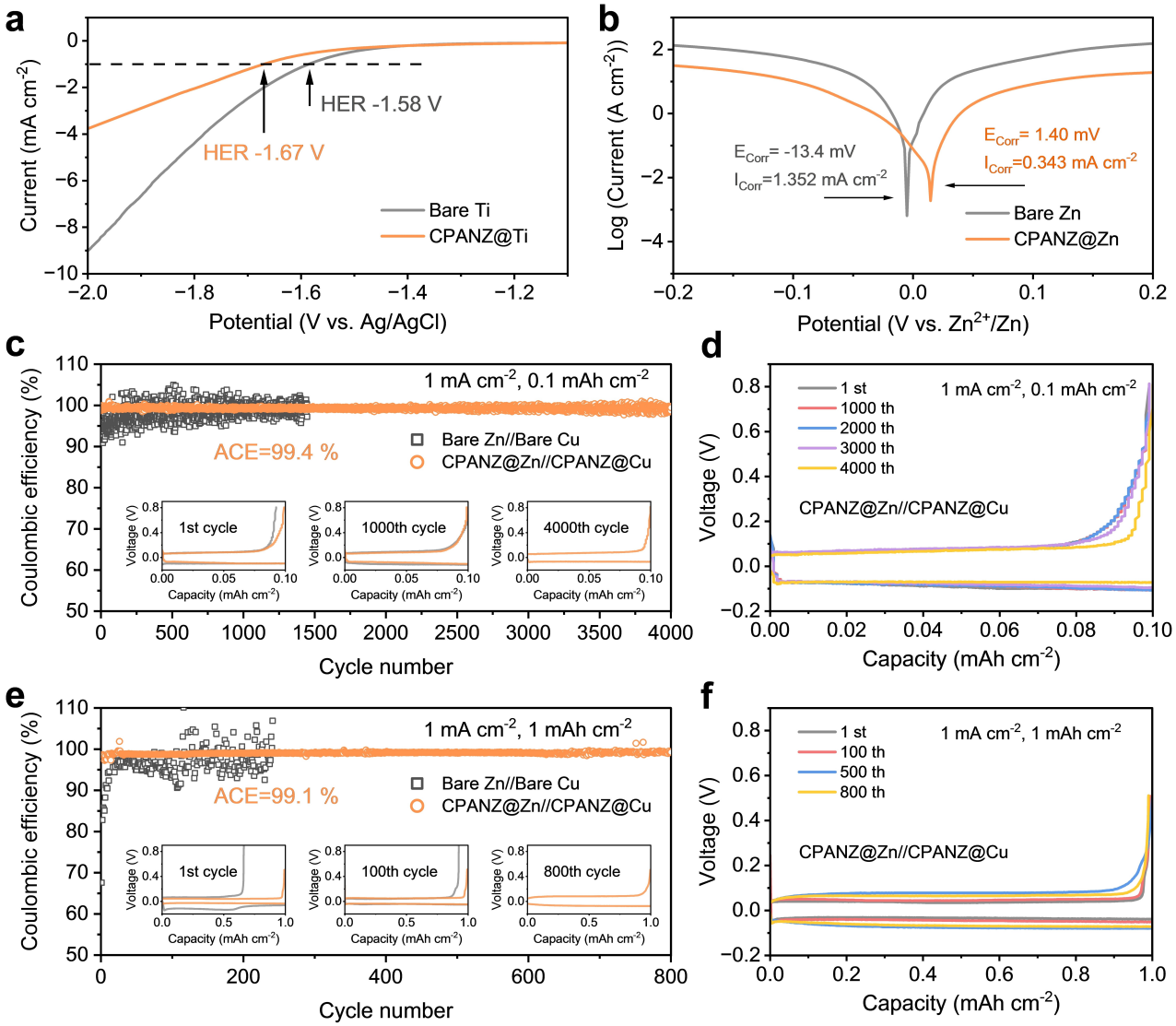

Figure 2. (a) Hydrogen evolution polarization curves of bare Ti and CPANZ@Ti in 1 M NaOTf. (b) Tafel curves showing the corrosion on bare Zn, and CPANZ@Zn. (c, e) Coulombic efficiency and (d, f) selected voltage-capacity profiles of Cu//Zn and CPANZ@Zn//CPANZ@Cu cells at 1 mA cm^{-2} and 0.1 mAh cm^{-2}, 1 mA cm^{-2} and 1 mAh cm^{-2}.

corrosion capabilities, leading to a prolonged cycle life for CPANZ@Zn//CPANZ@Cu cells. In addition, the formation of Zn dendrites and by-products is characterized to better understand the function of the localized conjugated CPANZ layer. The bare Zn anode exhibits a grey-coloured surface after cycling for 100 hours at a current density of 1 mA cm^{-2} with 1 mAh cm^{-2} (Figure S17), which is attributed to the by-product of $Zn_xOTF_y(OH)_{2x-y}{\cdot}nH_2O$ (ZOTFH). In contrast, the CPANZ@Zn maintains a dark-metal colour even after 1,000 hours. Noted that Zn is plated under the CPANZ layer due to the high ionic conductivity but low electric conductivity of the CPANZ layer (Figure S18). To ensure the clear observation of the morphology of Zn after cycling, the CPANZ layer was removed by etching using liquid nitrogen. The existence of ZOTFH in bare Zn anode is further confirmed by newly emerged peaks in X-ray diffraction (XRD) pattern (Figure S19), while only negligible by-products observed in the XRD spectra of CPANZ@Zn. Importantly, the intensity of the (002) peak in the CPANZ@Zn is stronger than that in bare Zn, indicating that the CPANZ layer is capable to regulating Zn growth along the (002) facet. This orientational growth can be attributed to the zincophilic effect of N-containing functional groups (–C=N–) in the CPANZ, leading to a regulated Zn deposition behaviour with a flat deposition morphology along with the (002) facet.[15] The distribution of by-products was further examined by the Microscope-FTIR spectra. Compared to the bare Zn (Figure 3a), the CPANZ@Zn anode exhibits a smooth and clean surface, with no obvious OH^- and CO_3^{2-} from the by-product detected (Figure 3b). This result demonstrates that the CPANZ is effective to suppress the Zn dendrite growth and by-product formation.

Additionally, Figure S20 shows that the nucleation overpotential (NOP) of CPANZ@Zn is 77 mV, higher than that of bare Zn at a scanning rate of 1 mV s^{-1}. The increased NOP facilitates the formation of smaller and denser nuclei, contributing to uniform Zn deposition.[16] This is supported by the suppressed 2D diffusion process and a more stable 3D diffusion process observed in the CPANZ@Zn (Figure 3c). The lower and more steady electrodeposition current suggests controlled and planar Zn growth. Figure 3d demonstrates the maximum stripping capacity of two electrodes at a current density of 1 mA cm^{-2}. Obviously, the cell using bare Zn exhibits a sudden increase in electrode polarisation when the total capacity reaches to 25.8 mAh cm^{-2}. This results from the uneven Zn stripping, leading to the formation of numerous unconnected pits and disruptions in the electronic network due to uncontrolled Zn^{2+} ion flux and serious side reactions on the surface. The loss of a conductive network results in the generation of numerous inactive Zn, contributing to severe capacity fading. This deteriorative effect becomes more pronounced when tested at a higher current density of 5 mA cm^{-2} (Figure S21). In contrast, cell using the CPANZ@Zn anode releases a higher total capacity value of 40.0 mAh cm^{-2}. The CPANZ modified layer enables even distribution of Zn^{2+} flux by the regulated Zn^{2+} migration channel, contributing to homogenized Zn stripping. The enlarged capacity in the CPANZ@Zn anode demonstrates that the CPANZ layer improves the behaviour of Zn stripping and plating. Additionally, the tensile strength of CPANZ is more than double that of PANZ (Figure S22). Such strength improvement helps to accommodate to the volume change during Zn electroplating/stripping and resist the penetration of Zn dendrite. Figure 3e shows that the peeling strength of the localized conjugated CPANZ layer is also higher than that of the PANZ layer. It maintains a comparable strength after Zn plating/stripping, indicating the good durability of the CPANZ layer on the Zn anode. The strong interfacial adhesion is attributed from the strong bonding between the conjugated –C=N from the CPANZ layer and Zn, as further evidenced by the stronger adsorption capability of CPANZ monomers on (002) and (101) Zn facets (Figure 3f). The improved peel resistance can alleviate the volume change during Zn plating/stripping (Figure S23), ensuring the long-lasting protective effect of the CPANZ interfacial layer.

Benefiting from the regulated Zn stripping/plating, mitigated side reactions and rapid Zn^{2+} diffusion kinetics, the lifespan of CPANZ@Zn//CPANZ@Zn cells is improved to 6,300 hours at a current density of 0.5 mA cm^{-2} with a capacity of 0.5 mAh cm^{-2}, which is 30 times longer than that of the bare Zn (Figure 4a). The slightly increase in electrode polarisation at ~2200 h is due to the sudden temperature change in the testing environment. The cycle life still exceeds 5,000 hours even at higher current densities of 1 and 3 mA cm^{-2} (Figure 4b and Figure S24), and the medium voltage in CPANZ@Zn anode can be stabilised at ±50 mV for more than 2,500 cycles at a current density of 3 mA cm^{-2} with a capacity of 3 mAh cm^{-2} (Figure 4c). In contrast, the voltage hysteresis of cell using bare Zn increases rapidly due to severe side reactions and the formation of by-products. Additionally, the CPANZ@Zn anode exhibits a better rate capability when compared to the bare Zn at similar current densities (Figure S25). The CPANZ@Zn anode also possesses good temperature-compatibility from 15 to 45 °C (Figure S26). The accelerated electrode kinetics at high temperatures is mainly attributed to two factors: the increased ionic conductivity of the electrolyte and the accelerated migration of Zn^{2+} within the CPANZ layer. Notably, the performance of the CPANZ@Zn electrode surpasses those of previously reported Zn anodes modified with different conductive layers (Figure 4d, e and Table S1).[17] Figure 4f, g show the morphology change of anodes after long-term cycling. The CPANZ@Zn electrode exhibits a more uniform and dendrite-free morphology, in contrast to the bare Zn, where large pits and protruding particles are observed. We further evaluated the practical feasibility of the CPANZ@Zn anode in AZIBs and zinc hybrid capacitors, coupled with 5,7,12,14-pentacenetetrone (PT) and active carbon (AC) cathodes, respectively. Figure 5a and Figure S27 display CV curves of the PT cathode coupled with CPANZ@Zn and bare Zn anodes, respectively. The result shows that the electrochemical behaviour of the PT cathode is not affected by the CPANZ layer. Two obvious reduction peaks, located at 0.52 and 0.2 V, and three oxidation peaks at 0.57, 0.73, and 0.88 V, respectively, are observed from all CV curves. The CV curves of

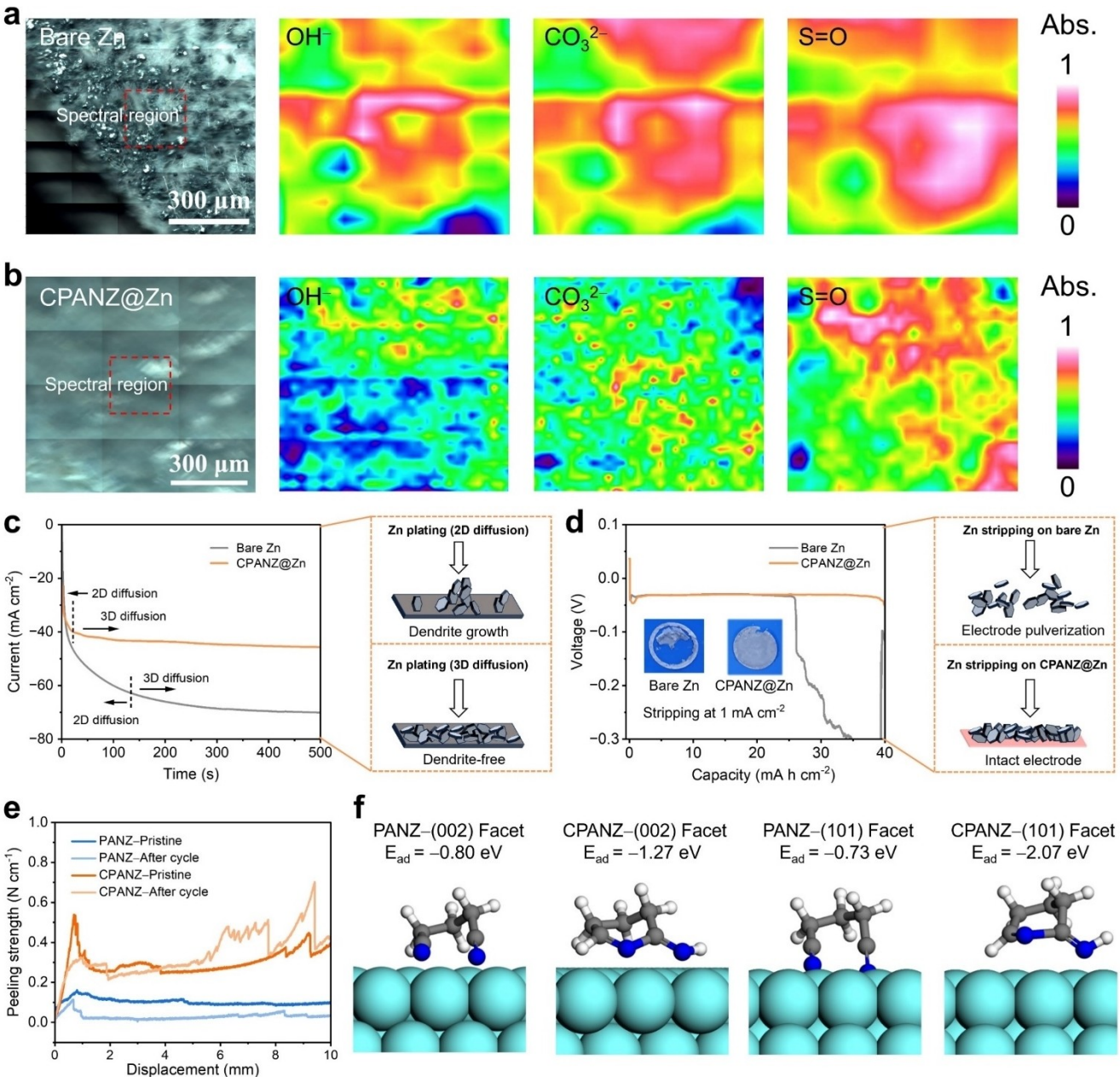

Figure 3. Micro-FTIR mapping of (a) bare Zn and (b) CPANZ@Zn anode after 100 h cycle at 1 mA cm^{-2} and 1 mAh cm^{-2}. (c) Chronoamperometry curves of bare Zn and CPANZ@Zn at an overpotential of −150 mV. The diagram (right) shows two different Zn plating patterns. (d) Capacity-voltage profiles of bare Zn//bare Zn cells and CPANZ@Zn//CPANZ@Zn cells, showing the maximum stripping capacity of bare Zn and CPANZ@Zn at 1 mA cm^{-2}. The diagram (right) shows two different Zn stripping patterns. (e) Peeling strength of coating layers on PANZ@Zn and CPANZ@Zn electrodes. (f) Absorption models of PANZ and CPANZ on the (002) and (101) Zn facets and corresponding absorption energy (E_{ad}).

CPANZ@Zn//PT cell maintains redox peaks at similar locations with increasing scanning rates, indicating the good reversibility of the cell (Figure S28). Moreover, the CPANZ@Zn//PT cell exhibits superior rate capability when compared with those in bare Zn//PT cells (Figure 5b), indicating the rapid Zn^{2+} transfer kinetics and restricted H^+ diffusion endowed by the CPANZ@Zn anode. Figure 5c shows that the cycle performance of CPANZ@Zn//PT cells at a current density of 0.5 A g^{-1} is improved, providing a stable lifespan of 900 cycles with high Coulombic efficiency values close to 100 %. In contrast, the bare Zn//PT cell can only operate after 340 cycles at the same test condition. Even at a current density of 2.0 A g^{-1}, the CPANZ@Zn//PT cell provides a capacity of 126.8 mAh g^{-1} with no capacity decay after 4,000 cycles (Figure 5d), while the bare Zn//PT cell only maintains a capacity lower than 80 mAh g^{-1} after 2000 cycles. Similarly, the CPANZ@Zn//AC capacitor also exhibits improved rate capability (Figure S29 and S30). The capacitor maintains a capacity retention of nearly 100 % after 10,000 cycles under a current density of 5.0 A g^{-1}

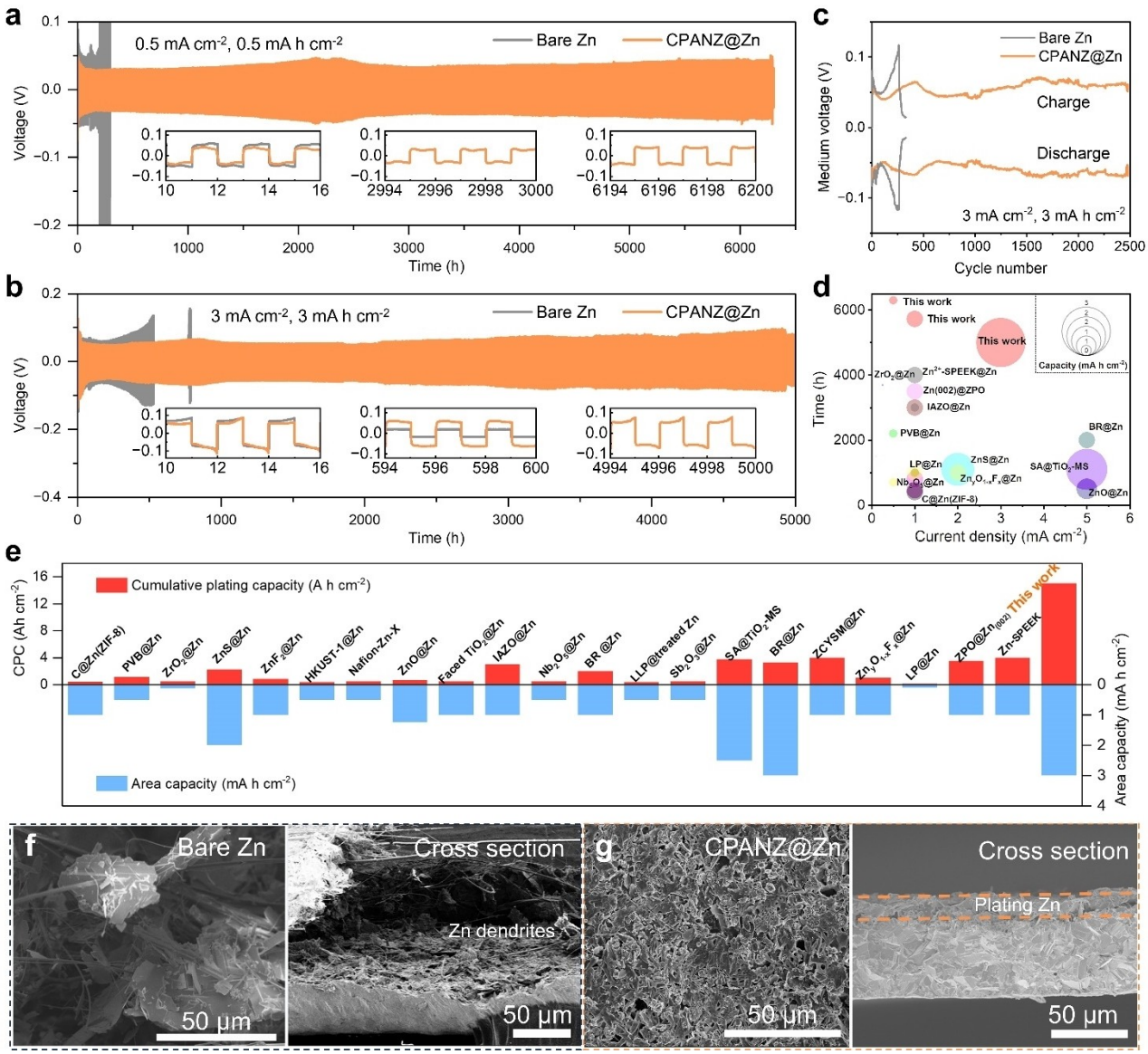

Figure 4. Cycling performance of Zn//Zn and CPANZ@Zn//CPANZ@Zn cells at (a) 0.5 mA cm^{-2} and 0.5 mAh cm^{-2} and (b) 3 mA cm^{-2} and 3 mAh cm^{-2}. (c) Medium voltage of Zn//Zn and CPANZ@Zn//CPANZ@Zn cells at 3 mA cm^{-2} and 3 mAh cm^{-2} (One cycle consists of consecutive 1 h charge and 1 h discharge process.). (d) Comparison of lifespan of CPANZ@Zn anode with previously reported modified Zn anodes. The diameter of circles represents the testing capacity. (e) Comparison of cumulative plating capacity (CPC) and area capacity of CPANZ@Zn anode with previously reported modified Zn anodes. SEM images of (f) bare Zn and (g) CPANZ@Zn after 100 h cycle at 1 mA cm^{-2} and 1 mAh cm^{-2}.

(Figure S31), demonstrating the good cathode compatibility of the CPANZ@Zn anode. The practical applicability of CPANZ@Zn is further exemplified through its integration into the CPANZ@Zn//PT pouch cell. In contrast to the fast deterioration observed in the bare Zn//PT pouch cell, the CPANZ@Zn//PT pouch cell demonstrates remarkable stability. It maintains a consistently high CE close to 100 % over 200 cycles, concurrently exhibiting an impressive capacity retention rate of 93.08 % (Figure 5e). This disparity underscores the enhanced durability and sustained functionality achieved through the incorporation of CPANZ@Zn in the pouch cell configuration.

Conclusion

In this work, we induced the formation of localized conjugated structures of PAN at low temperatures by Lewis acidic $Zn(OTf)_2$ and designed a cyclized polyacrylonitrile Zn anode modified interfacial layer (CPANZ) with this localized conjugated layer. The CPANZ effectively inhibits irreversible corrosion, HER and other side reactions at the Zn anode and achieves uniform Zn deposition by regulating Zn^{2+} transport. The CPANZ@Zn anode provides high CE (ACE of 99.36 % for 4,000 cycles at 1 mA cm^{-2}), high cycling stability (5,750 h at 1 mA cm^{-2}/1 mAh cm^{-2}; 5,000 h at 3 mA cm^{-2}/3 mAh cm^{-2}), realizing an exceptional cumulative capacity of over 15 A h cm^{-2}. The full battery assembled with

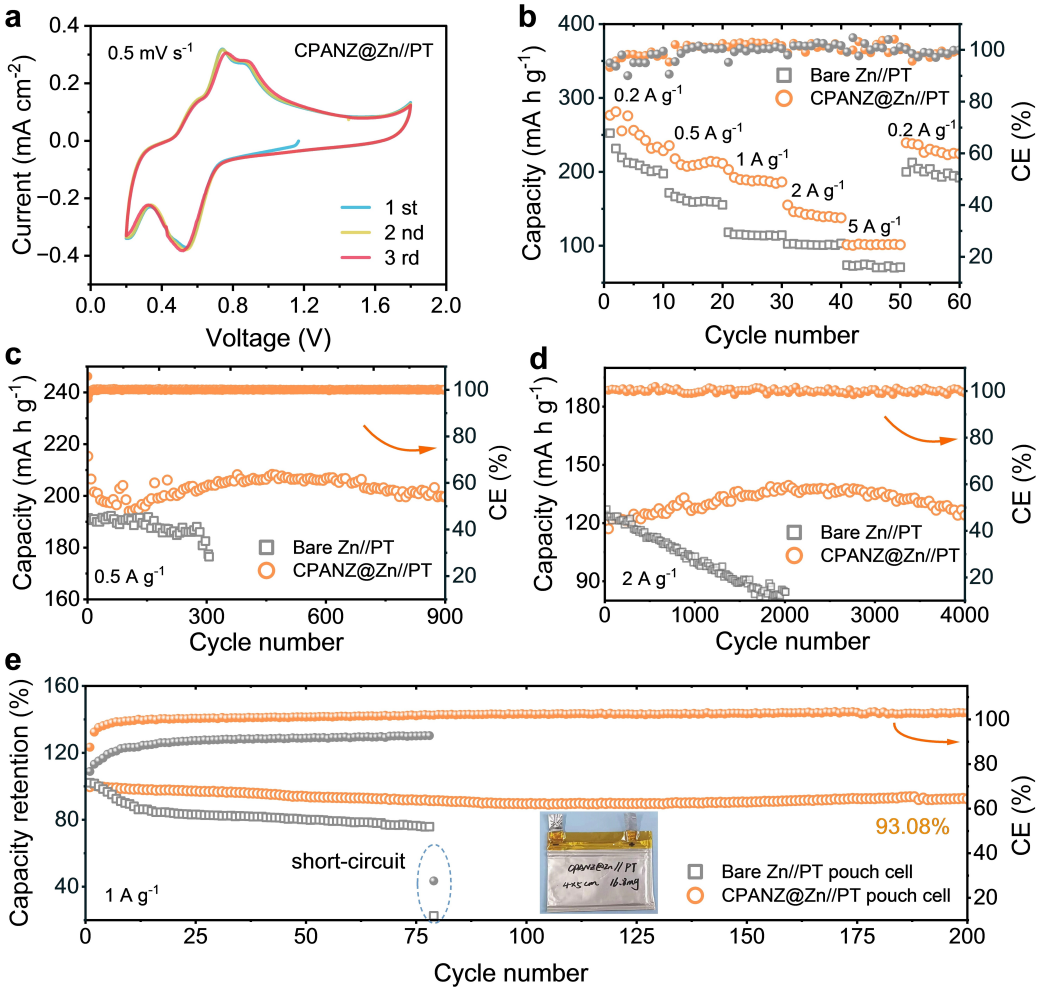

Figure 5. (a) CV curves of CPANZ@Zn//PT cells at a scanning rate of 0.5 mV s^{-1}. (b) Rate capability of bare Zn//PT and CPANZ@Zn//PT cells. Cycling performance of bare Zn//PT and CPANZ@Zn//PT cells (c) at 0.5 A g^{-1} and (d) at 2 A g^{-1}. (e) Cycling performance of bare Zn//PT and CPANZ@Zn//PT pouch cells of at 1 A g^{-1}. Inset shows the optical photo of the pouch cell.

PT cathode can be cycled 4,000 times at 2 A g^{-1} with capacity retention and CE close to 100 %. The assembled ZHCs also demonstrated stable cycling over 10,000 cycles. The CPANZ@Zn//PT pouch cell maintained a capacity retention of 93.08 % with nearly 100 % CE after 200 cycles, further demonstrating the superior stability of the localized conjugated CPANZ layer.

Supporting Information

The authors have cited additional references within the Supporting Information.[18]

Acknowledgements

Z. J. L., G. J. L. and M. R. X. are contributed equally to this work. This work was financially supported by the National Natural Science Foundation of China (52162036, 21965034, U1903217, and 22378342), the Key Project of Nature Science Foundation of Xinjiang Province (2021D01D08), the Xinjiang Autonomous Region Major Projects (2022A01005-4 and 2021A01001-1). G. J. L. was supported by scholarships from the China Scholarship Council (Grant No. 202006750014). Z. Guo acknowledges the financial support from the Australian Research Council (FL210100050). C. Zhang acknowledges the financial support from the National Natural Science Foundation of China (52172173). S. Zhang acknowledges the financial support from the Australian Research Council (DE240100159). S. Zhang would also like to thank the Australian Institute of Nuclear Science and Engineering (AINSE) for providing financial assistance through the Early Career Researcher Grant (ECRG). Open Access publishing facilitated by The University of Adelaide, as part of the Wiley - The University of Adelaide agreement via the Council of Australian University Librarians.

Conflict of Interest

The authors declare no conflict of interest.

Data Availability Statement

The data that support the findings of this study are available from the corresponding author upon reasonable request.

Keywords: Zn anode · zinc ion conductor · cyclization of polyacrylonitrile · aqueous zinc ion batteries

[1] R. J. Leicester, V. G. Newman, J. K. Wright, *Nature* **1978**, *272*, 518–521.
[2] a) C. Li, S. Jin, L. A. Archer, L. F. Nazar, *Joule* **2022**, *6*, 1733–1738; b) J. R. Miller, *Science* **2012**, *335*, 1312–1313.
[3] a) Q. Yang, L. Li, T. Hussain, D. Wang, L. Hui, Y. Guo, G. Liang, X. Li, Z. Chen, Z. Huang, Y. Li, Y. Xue, Z. Zuo, J. Qiu, Y. Li, C. Zhi, *Angew. Chem. Int. Ed.* **2022**, *61*, e202112304; b) G. Li, Z. Zhao, S. Zhang, L. Sun, M. Li, J. A. Yuwono, J. Mao, J. Hao, J. Vongsvivut, L. Xing, C.-X. Zhao, Z. Guo, *Nat. Commun.* **2023**, *14*, 6526; c) C. Zhang, H. Li, X. Zeng, S. Xi, R. Wang, L. Zhang, G. Liang, K. Davey, Y. Liu, L. Zhang, S. Zhang, Z. Guo, *Adv. Energy Mater.* **2022**, *12*, 2202577; d) J. Zhou, S. Zhang, Y.-N. Zhou, W. Tang, J. Yang, C. Peng, Z. Guo, *Electrochem. Energy Rev.* **2021**, *4*, 219–248.
[4] a) J. Wan, R. Wang, Z. Liu, L. Zhang, F. Liang, T. Zhou, S. Zhang, L. Zhang, Q. Lu, C. Zhang, Z. Guo, *ACS Nano* **2023**, *17*, 1610–1621; b) R. Wang, Q. Ma, L. Zhang, Z. Liu, J. Wan, J. Mao, H. Li, S. Zhang, J. Hao, L. Zhang, C. Zhang, *Adv. Energy Mater.* **2023**, *13*, 2302543.
[5] Q. Guan, Y. Li, X. Bi, J. Yang, J. Zhou, X. Li, J. Cheng, Z. Wang, B. Wang, J. Lu, *Adv. Energy Mater.* **2019**, *9*, 1901434.
[6] a) Q. Zhang, J. Luan, Y. Tang, X. Ji, H. Wang, *Angew. Chem. Int. Ed.* **2020**, *59*, 13180–13191; b) S. Zhao, Y. Zhang, J. Li, L. Qi, Y. Tang, J. Zhu, J. Zhi, F. Huang, *Adv. Mater.* **2023**, *35*, 2300195; c) C. Wang, J. Z. J. Zhu, S. Vi-Tang, B. Peng, C. Ni, Q. Li, X. Chang, A. Huang, Z. Yang, E. J. Savage, S. Uemura, Y. Katsuyama, M. F. El-Kady, R. B. Kaner, *Adv. Mater.* **2024**, *36*, 2306145.
[7] D. Wang, Q. Li, Y. Zhao, H. Hong, H. Li, Z. Huang, G. Liang, Q. Yang, C. Zhi, *Adv. Energy Mater.* **2022**, *12*, 2102707.
[8] D. Han, Z. Wang, H. Lu, H. Li, C. Cui, Z. Zhang, R. Sun, C. Geng, Q. Liang, X. Guo, Y. Mo, X. Zhi, F. Kang, Z. Weng, Q.-H. Yang, *Adv. Energy Mater.* **2022**, *12*, 2102982.
[9] a) H. N. Friedlander, L. H. Peebles Jr., J. Brandrup, J. R. Kirby, *Macromolecules* **1968**, *1*, 79–86; b) W.-P. Chen, H. Duan, J.-L. Shi, Y. Qian, J. Wan, X.-D. Zhang, H. Sheng, B. Guan, R. Wen, Y.-X. Yin, S. Xin, Y.-G. Guo, L.-J. Wan, *J. Am. Chem. Soc.* **2021**, *143*, 5717–5726; c) M. S. A. Rahaman, A. F. Ismail, A. Mustafa, *Polym. Degrad. Stab.* **2007**, *92*, 1421–1432.
[10] a) N. Medishetti, C. Ittamalla, J. B. Nanubolu, K. Atmakur, *Chem Select* **2022**, *7*, e202200063; b) P. Tong, Z. Sun, S. Wang, Y. Zhang, Y. Li, *J. Org. Chem.* **2019**, *84*, 13967–13974.
[11] a) R. B. Mathur, O. P. Bahl, J. Mittal, *Carbon* **1992**, *30*, 657–663; b) K. Badii, J. S. Church, G. Golkarnarenji, M. Naebe, H. Khayyam, *Polym. Degrad. Stab.* **2016**, *131*, 53–61.
[12] C. Lin, S.-H. Kim, Q. Xu, D.-H. Kim, G. Ali, S. S. Shinde, S. Yang, Y. Yang, X. Li, Z. Jiang, J.-H. Lee, *Matter* **2021**, *4*, 1287–1304.
[13] a) Q. Zhang, J. Luan, L. Fu, S. Wu, Y. Tang, X. Ji, H. Wang, *Angew. Chem. Int. Ed.* **2019**, *58*, 15841–15847; b) A. Bayaguud, X. Luo, Y. Fu, C. Zhu, *ACS Energy Lett.* **2020**, *5*, 3012–3020.
[14] a) S. Lei, Z. Zeng, M. Liu, H. Zhang, S. Cheng, J. Xie, *Nano Energy* **2022**, *98*, 107265; b) J. Yang, J. Ruan, Q. Li, F. Fang, Y. Song, D. Sun, F. Wang, *Adv. Funct. Mater.* **2022**, *32*, 2200566.
[15] J. Zhou, M. Xie, F. Wu, Y. Mei, Y. Hao, R. Huang, G. Wei, A. Liu, L. Li, R. Chen, *Adv. Mater.* **2021**, *33*, 2101649.
[16] a) F. Yang, J. A. Yuwono, J. Hao, J. Long, L. Yuan, Y. Wang, S. Liu, Y. Fan, S. Zhao, K. Davey, Z. Guo, *Adv. Mater.* **2022**, *34*, 2206754; b) D. Xie, Z.-W. Wang, Z.-Y. Gu, W.-Y. Diao, F.-Y. Tao, C. Liu, H.-Z. Sun, X.-L. Wu, J.-W. Wang, J.-P. Zhang, *Adv. Funct. Mater.* **2022**, *32*, 2204066.
[17] a) C. Shen, X. Li, N. Li, K. Xie, J.-g. Wang, X. Liu, B. Wei, *ACS Appl. Mater.* **2018**, *10*, 25446–25453; b) M. Liu, L. Yang, H. Liu, A. Amine, Q. Zhao, Y. Song, J. Yang, K. Wang, F. Pan, *ACS Appl. Mater.* **2019**, *11*, 32046–32051; c) R. Yuksel, O. Buyukcakir, W. K. Seong, R. S. Ruoff, *Adv. Energy Mater.* **2020**, *10*, 1904215; d) J. Hao, X. Li, S. Zhang, F. Yang, X. Zeng, S. Zhang, G. Bo, C. Wang, Z. Guo, *Adv. Funct. Mater.* **2020**, *30*, 2001263; e) W. Yang, B. Ling, B. Hu, H. Yin, J. Mao, P. J. Walsh, *Angew. Chem. Int. Ed.* **2020**, *59*, 2–2; f) X. Xie, S. Liang, J. Gao, S. Guo, J. Guo, C. Wang, G. Xu, X. Wu, G. Chen, J. Zhou, *Energy Environ. Sci.* **2020**, *13*, 503–510; g) Q. Zhang, J. Luan, X. Huang, Q. Wang, D. Sun, Y. Tang, X. Ji, H. Wang, *Nat. Commun.* **2020**, *11*, 3961; h) H. Zhang, Y. Wu, J. Yu, T. Jiang, M. Wu, *Adv. Funct. Mater.*, *n/a*, 2301912; i) H. Fan, M. Wang, Y. Yin, Q. Liu, B. Tang, G. Sun, E. Wang, X. Li, *Energy Storage Mater.* **2022**, *49*, 380–389; j) N. Guo, Z. Peng, W. Huo, Y. Li, S. Liu, L. Kang, X. Wu, L. Dai, L. Wang, S. C. Jun, Z. He, *Small* **2023**, *19*, 2303963.
[18] a) G. Kresse, J. Furthmüller, *Phys. Rev. B* **1996**, *54*, 11169–11186; b) P. E. Blöchl, *Phys. Rev. B* **1994**, *50*, 17953–17979; c) J. P. Perdew, K. Burke, M. Ernzerhof, *Phys. Rev. Lett.* **1996**, *77*, 3865–3868; d) Y. Zhang, W. Yang, *Phys. Rev. Lett.* **1998**, *80*, 890–890; e) S. Grimme, J. Antony, S. Ehrlich, H. Krieg, *J. Chem. Phys.* **2010**, *132*, 154104.

Manuscript received: December 11, 2023
Accepted manuscript online: February 2, 2024
Version of record online: February 20, 2024